Hybrid-Electric Rotorcraft Sizing with Detailed Engine Specific Fuel Consumption

Matthew Arace* and Anubhav Datta†
University of Maryland, College Park, Maryland 20742
and
Michael Ricci‡
LaunchPoint EPS, Goleta, California 93117

https://doi.org/10.2514/1.C038404

Data from a 4.5 hp piston engine generator is integrated with rotorcraft sizing to assess its impact. First, the specific fuel consumption (SFC) map of the powerplant is measured and modeled. Second, a sizing loop is developed for vertical take-off and landing (VTOL) aircraft and calibrated with XV-15 flight test aircraft and a NASA conceptual electric-VTOL aircraft. The power and platform models are then integrated to size a quadrotor biplane unmanned air vehicle of 5 lb payload. Several cases on how the engine speed can be controlled to meet the vehicle torque and speed are detailed. The key conclusion is that a detailed SFC model is as important as the rotor aeromechanics model. Without a detailed SFC model, errors in gross weight and range can be as high as 100%, due to incorrect tip speed reduction. With a detailed SFC model, a tip speed reduction of 30–40% is optimal to maximize the range of a 50 lb aircraft. The resulting aircraft has a minimum gross weight of 50 lb and a maximum range of 37 nm at 60 kt cruise speed.

Nomenclature

a_G	=	acceleration due to gravity, m/s^2
$A_0 - A_3$	=	nondimensional engine model constants for losses
$B_0 - B_{15}$	=	nondimensional engine model constants for indicated thermal efficiency (full model)
$b_0 - b_2$	=	nondimensional engine model constants for indicated thermal efficiency (linear range)
$bmep$	=	brake mean effective pressure, Pa
D	=	drag, N
f	=	third-order function in engine speed
$fmep$	=	friction mean effective pressure, Pa
g	=	3rd order function in engine torque
I	=	current, A
L	=	lift, N
$\dot{m}_f$	=	fuel mass flow rate, kg/h
NCV	=	net calorific value of fuel, (kW · h)/kg
n_c	=	output revolutions/cycle (equal to 2 for four-stroke engine)
P	=	power, kW
P_{Eng}	=	engine power, W
P_{Gen}	=	generator power, W
$pmep$	=	pumping mean effective pressure, Pa
Q	=	torque, N · m
Q_E	=	engine torque, N · m
$\overline{Q}_E$	=	nondimensional torque
$Q_{E_{\max}}$	=	maximum continuous engine torque, N · m
SFC	=	specific fuel consumption, kg/(kW · h)
v	=	velocity, m/s
V	=	voltage, V
V_S	=	swept cylinder volume, m^3
W	=	weight, kg
η_G	=	generator efficiency
η_B	=	brake thermal efficiency
η_M	=	mechanical efficiency
η_T	=	indicated thermal efficiency
Ω_E	=	engine rotational speed, rad/s
$\overline{\Omega}_E$	=	nondimensional engine rotation speed
$\Omega_{E_{\max}}$	=	maximum continuous engine speed, rad/s

Received 27 January 2025; accepted for publication 14 June 2025; published online 9 September 2025.

*Graduate Research Assistant, Department of Aerospace Engineering; marace@umd.edu. Student Member AIAA.

†Associate Professor, Department of Aerospace Engineering; datta@umd.edu. Associate Fellow AIAA.

‡CTO, LaunchPoint EPS, 320 Storke Road.

I. Introduction

IN RECENT years there has been an increased interest in distributed propulsion and multirotor aircraft. Large-scale multirotor concepts have been prototyped in the past, but all suffered from severe issues stemming from complexity of the mechanical power transmission and the associated weight penalty, such as the X-19 [1] and X-22 [2]. An electrical power transmission may alleviate these problems and also enable independent rotor speed control. However, low-energy densities of battery packs (typically 200–250 W·h/kg) severely limits the range and payload of battery-electric vehicles. Hybrid-electric power can bridge this vehicle performance gap, using the high-energy density of traditional fuel while reaping the benefits of a distributed propulsion system.

Even though there is a vast amount of literature on hybrid-electric power for automobiles, see textbooks such as Refs. [3,4] for example, the vertical takeoff and landing (VTOL) aircraft is fundamentally different. The design principal in automobiles, regenerative braking, is no longer practical; instead, there is the promise of enabling the partial or complete elimination of mechanical drivetrains to enable aircraft for which mechanical actuation is impractical.

Literature on hybrid-electric aircraft has been emerging in the last decade [5,6], but most, if not all, are conceptual explorations. Fixed-wing aircraft were initially the focus, while interest for VTOL has gained more traction in recent years [7]. The test data for reliable assessment of these concepts are limited. The 1500 lb Moog Workhorse SureFly hybrid-electric quadrotor flew in 2018, but few details were published [8]. The hybrid-electric quad-tilt-prop LC62-50H was also flown around 2020, but even fewer details are available. The goal of this research is to address this gap by producing experimental data and applying it to aircraft analysis.

The size of the present test bed is loosely based on a 50 lb conceptual quadrotor biplane tailsitter (QBIT) design of Sridharan et al. [9], shown in Fig. 1, which is a configuration similar to the 55 lb Bell Autonomous Pod Transport (APT) 20. The QBIT is a special unmanned aerial vehicle (UAV) that is capable of high-

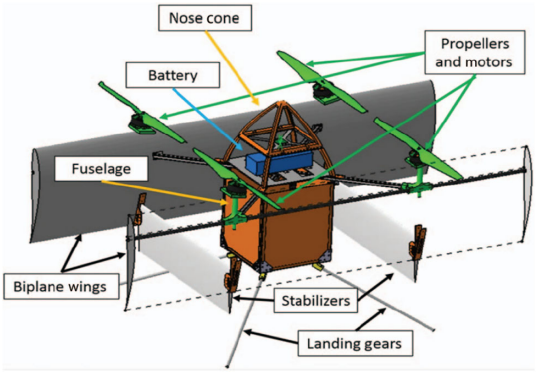

Fig. 1 Example QBIT from Ref. [9].

efficiency hover *and* cruise without any tilting mechanisms for the rotors. The conceptual study showed the advantages of a piston-electric hybrid for significant range extension over batteries, but there were no test data at the time. They recommended a two-stroke engine with a budget of 10 kg and maximum continuous power 2.5 kW. Earlier work focused on building and testing such a two-stroke engine rig [10], but the test data were not fed back into design, nor was the system integrated on an aircraft. They also recommended a larger four-stroke engine for higher efficiency. In 2022, Ricci et al. [11] demonstrated such systems can indeed be integrated onboard to fly multirotor UAV. The present work is inspired by these developments and focuses on an experimental exploration of four-stroke engine performance and the impact of test data on the conceptual design of a QBIT.

In this paper, hybrid-electric is defined as a power plant where a combustion engine is the power source and a generator converts the mechanical power to electrical for transmission and delivery to the electric motors that drive the rotors. A rectifier is used to convert the ac output of the generator to dc. This allows for independent control of each rotor and for the power to be supplemented by a battery downstream if desired. A simple schematic of the power plant is shown in Fig. 2 with one rotor as the load.

The objectives of this paper are to fabricate, test, and understand power generation of a 3.43 kW four-stroke piston engine coupled to a generator and use these data to size a 50 lb QBIT. The fuel efficiency of the power plant is characterized by the overall specific fuel consumption (SFC). Isolated engine/generator tests are carried out using an electrical load bank to map the entire engine operating range without stalling the rotors. The measurements include fuel mass flow $\dot{m}_f$, engine speed Ω_E and torque and Q_E, and generator voltage (V) and current (I). From these measurements, specific fuel consumption and generator efficiency are determined. The SFC of the isolated engine is characterized and understood. The characterization of the electrical efficiency and overall SFC of the engine/generator set are documented in Ref. [12]. A phenomenological model is developed and calibrated with the experimental data to predict the fuel consumption of the isolated engine. This model is used in an aircraft sizing exercise for a 50 lb quadrotor biplane. Preliminary results are reported in Refs. [12,13]. The final results are archived in this paper.

In sizing this vehicle, a judicious reduction in rpm in cruise can buy very high range [14]. The thrust required in cruise for a VTOL aircraft, especially with a wing, is significantly reduced. The fundamental principle is that if the airspeed over the blade is reduced the blades must operate at higher, more efficient, angles of attack to produce equivalent thrust. Conventional combustion engines are unable to provide a dramatic reduction in rpm on their own. Although a two-speed gearbox is possible, the result is a much more complex mechanical transmission. An electric transmission can alleviate many of the problems that accompany a complex mechanical transmission, hence the promise of hybrid electric. How much rpm reduction is needed in cruise, however, remains unclear. The best method of achieving the rpm reduction also remains unclear. This endeavor focuses on higher-fidelity prediction of fuel consumption and how a detailed SFC prediction impacts the design choices to minimize weight. Different methods to achieve the rpm reduction for the rotor in cruise are also explored.

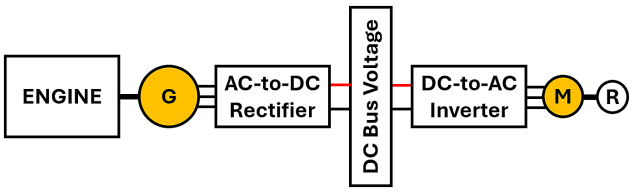

Fig. 2 Simple schematic of power flow; G = generator, M = motor, R = rotor.

II. Test Setup

The test setup is shown in Fig. 3. A four-stroke engine (Saito FG61-TS) is connected to a shaft-to-shaft torque transducer. The other end of the transducer is connected to a generator. The three-phase ac output from the generator is connected to an ac/dc rectifier, which is then directly connected to a constant current electrical load bank (Eagle Eye LB-48-200-CC). The engine is mounted to a 3/4-in.-thick plywood firewall for vibration damping, and the system is mounted to a 6115 aluminum test frame.

The engine fits within the power and weight budget of the conceptual aircraft. It is an opposing twin cylinder internal combustion engine weighing 2.26 kg with a maximum continuous power of 3.43 kW. The engine uses a fuel/oil mix and therefore does not require separate lubrication. The engine was tuned to achieve a maximum rotational speed of 7000 rpm. An ignition module and shaft-mounted Hall-effect sensor powered by an external battery control the firing of the spark plugs. Air cooling is provided by an industrial fan pointed directly at the engine. This mimics the air cooling that would typically be provided by the downwash of a propeller fixed to the engine shaft. To start the engine in this configuration, two additional components were required. Typically, a propeller mounted to the shaft of the engine provides enough rotational inertia to complete the compression stroke in each cycle. In the test setup, the shaft is rigidly connected to the generator and therefore lacks the necessary inertia to sustain operation, so a flywheel is machined and attached inline to the shaft. Engines of this class rely on hand starting by flipping the propeller. This is not possible in the test setup as the end of the engine shaft is not free. Therefore, a pull-start mechanism is incorporated by wrapping a rope around the shaft and pulling it through several revolutions. When primed correctly, the cylinders will fire, and the engine will start.

The generator (KDE8218XF-120) is a brushless dc motor with trapezoidal signals configured to absorb torque and output current. The generator is rated for a maximum continuous power of 5.7 kW at 110 A and has a motor velocity constant of 120 rpm/V and a motor torque constant of 0.0796 $(\mathrm{N}\cdot\mathrm{m})/\mathrm{A}$.

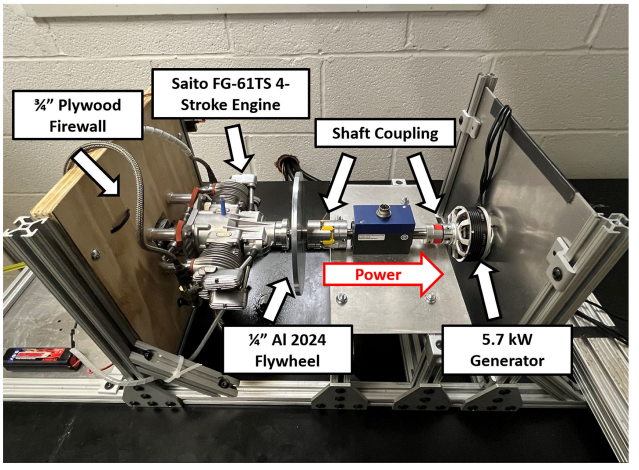

Fig. 3 A four-stroke piston-electric rig.

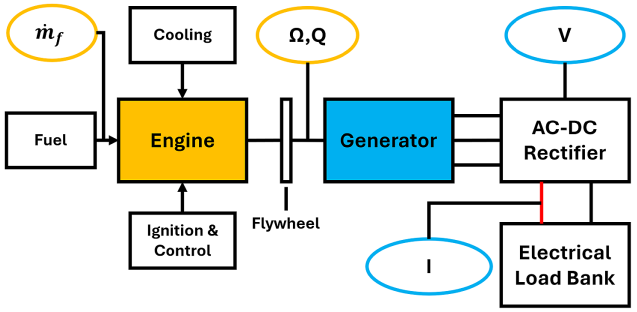

Fig. 4 Block diagram of hardware and instrumentation. I is current, V is voltage, Ω is engine speed, Q is engine torque, and $\dot{m}_f$ is fuel mass flow from tank.

The ac/dc rectifier is a three-phase, six-diode bridge rectifier. It converts the incoming three-phase ac from the generator to dc output. The rectifier is rated for 200 A dc and a maximum rms voltage of 1600 V_{rms}. A block diagram of the hardware and instrumentation is shown in Fig. 4. The rectangles in the block diagram represent hardware components and the ellipses represent instrumentation.

A National Instruments data acquisition system (DAQ) was used with LabVIEW as the software. A scale with ±1 g precision is used to measure fuel consumed during each test. Engine rotational speed Ω_E is measured using a Hall-effect sensor mounted to the engine shaft. The Hall-effect sensor is connected to a tachometer to display rpm during operation. Engine torque Q_E is measured using a HBM T21WN transducer powered by a 10 V dc power supply. The dc voltage V and current I are measured postrectification. An 11:1 voltage divider is fabricated to reduce the voltage signal to the DAQ's acceptable range. The current is measured from the positive lead of the load bank using an Allegro ACS-700LCB-100U-PFF-T Hall-effect sensor powered by a 5 V dc power supply. The current passed through the sensor generates a magnetic field, and the sensor outputs a constant square wave voltage based on the strength of the magnetic field. The current sensor is attached inline with the positive lead of the load bank. The output signal from the current sensor passes through a second-order resistor-capacitor (RC) filter, or a low-pass filter, to convert the output Pulse width modulation (PWM) signal to a constant analog voltage value prior to passing to the DAQ. Data are collected at a rate of 2 kHz. The engine rpm and current drawn are independent and can be specified at will. This is a unique feature of the rig. This setup is open loop with manual throttle control as conducive to parametric studies. The rpm is held constant for each test point manually through the tachometer.

The true rpm is extracted from the frequency content of the torque signal. The engine power is subsequently obtained as $P_E = Q\Omega_E$ and generator power is obtained from $P_G = VI$. The specific fuel consumption is $SFC = \dot{m}_f/P_E$, and the generator efficiency is $\eta_G = P_G P_E$.

III. Test Procedure

Data are collected for the test cases shown in Fig. 5. The following sequence is executed for each case:

1) The engine is started using the external pull start and allowed to warm for 1 min.

2) The rpm is adjusted to high idle, and the current load is set using the load bank. For the higher current cases, the current must be drawn gradually to allow the engine to react and supply the required torque. If too much torque is required instantaneously, the engine or powertrain components could be damaged. Therefore, the current drawn is increased in steps of 10 A up to the desired value.

3) The engine rpm is adjusted to the desired set point.

4) The fuel weight is recorded, and data acquisition is initiated.

5) Data are collected until 20 g of fuel is consumed. Then, the engine is shut down and allowed to cool.

6) The instantaneous data collected are averaged to return a single value of rpm, torque, current, and voltage. The efficiency metrics are then calculated.

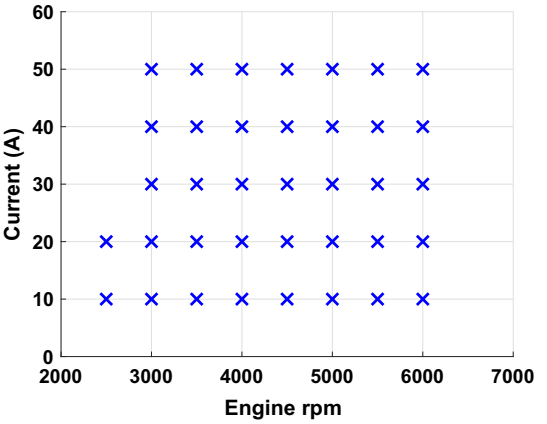

Fig. 5 Test points collected.

IV. Experimental Results

The measured data are tabulated in Table 1. The mechanical power, electrical power, generator efficiency, and SFC can be calculated from this data. Of these, the most important metric is the SFC.

The SFC is plotted with respect to engine rpm and torque in Fig. 6. The efficiency islands appear clearly. Parametric curves are used to close the islands. To find the curves, the data are analyzed for two cases: constant torque and constant rpm. At a constant torque, the engine fuel mass flow $\dot{m}_f$ follows a cubic variation in rpm (an example is shown in Fig. 7a). Similarly, at a constant engine speed, $\dot{m}_f$ follows a cubic variation in torque (an example is shown

Table 1 Test data collected

Engine speed RPM	Current A	Voltage V	Torque N · m	Fuel mass flow rate kg/h
2530	10.08	16.48	0.784	0.474
2537	20.55	15.55	1.453	0.474
3030	10.09	19.91	0.786	0.518
3010	20.09	18.19	1.426	0.522
3030	30.55	16.91	2.015	0.426
3073	41.69	15.70	2.603	0.466
3093	50.22	14.37	3.008	0.507
3423	10.07	22.74	0.794	0.563
3454	20.44	21.15	1.427	0.581
3432	30.25	19.53	1.987	0.456
3673	40.67	19.44	2.532	0.467
3681	51.17	17.83	3.003	0.571
3997	10.12	26.65	0.797	0.580
3963	20.66	24.05	1.455	0.573
4078	30.43	23.66	2.040	0.504
4046	40.68	21.86	2.553	0.490
3969	50.12	19.64	2.990	0.589
4441	10.16	29.71	0.829	0.590
4501	20.25	28.11	1.439	0.590
4505	30.42	26.43	2.050	0.507
4569	40.45	25.22	2.568	0.554
4534	50.10	22.86	2.991	0.643
4997	10.18	34.50	0.843	0.645
4995	20.34	32.04	1.450	0.611
4998	30.21	29.76	2.021	0.525
4998	40.34	27.88	2.622	0.643
4996	50.06	26.97	2.990	0.790
5579	10.18	38.44	0.848	0.655
5508	20.43	35.01	1.465	0.621
5563	30.53	33.26	2.061	0.655
5568	40.94	31.46	2.643	0.776
5440	50.77	27.80	3.016	0.969
6000	10.17	40.72	0.855	0.655
6025	22.06	39.08	1.508	0.600
6018	31.07	36.42	2.066	0.762
6004	41.70	34.18	2.640	0.919
6014	50.50	31.82	3.012	1.161

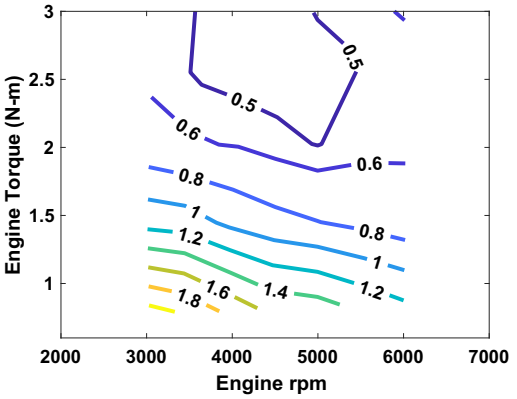

Fig. 6 Engine SFC (kilograms/kilowatt hour) raw data contour.

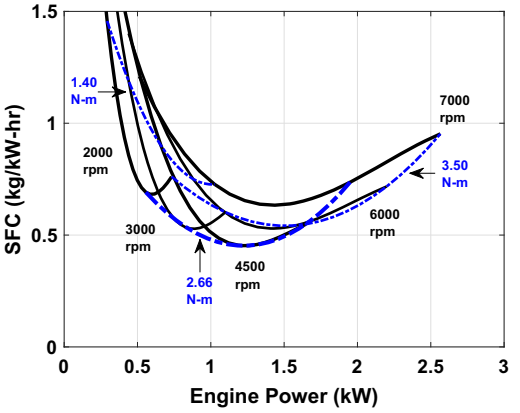

Fig. 9 Engine SFC versus engine power with constant rpm lines.

in Fig. 7b). The SFC is replotted in Fig. 8a. The variation is now smooth, and the islands close. Next, based on the clear trends shown in Fig. 7, the rpm range is extended to 2000–7400 rpm and the torque range to 0.8–4.4 N · m to cover the entire range of engine operation, beyond what the equipment used could measure. These extreme regions minimally impact the calibration of the model later. The extrapolated contour is shown in Fig. 8b. Minimum SFC is observed around 4500 rpm and 2.6 N · m of torque.

The same data are plotted versus power in Fig. 9. The constant rpm lines are solid, and the constant torque lines are dashed. It is clear that SFC is a function of both rpm and torque, not just power. At any desired power, there is a single combination of rpm and torque where the SFC is minimized.

A similar exercise is conducted for the generator efficiency. A nonlinear surface is fit to the power lost from conversion. The generator efficiency plot for the same torque and rpm range is shown in Fig. 10. The generator efficiency islands are different than the SFC islands. The combination of these islands represent the efficiency of the power source. These SFC and generator efficiency maps are used for aircraft sizing in Sec. VI.

V. Mathematical Model

Although table look-up can be used for sizing, a mathematical model is needed for scaling. Generator and motor models are well developed in literature, such as Ref. [15], so attention is devoted

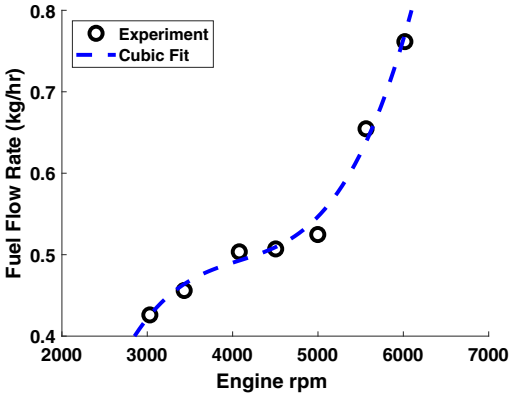

a) Engine fuel mass flow rate with rpm at 2.0 N-m torque

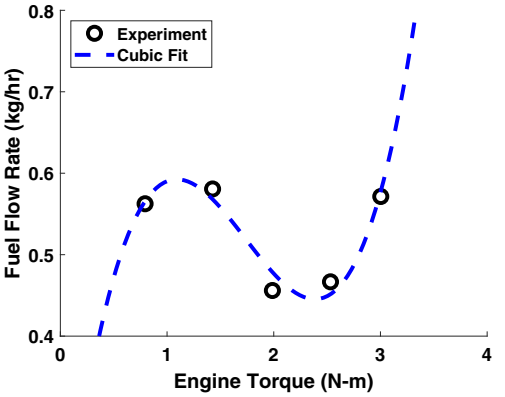

b) Engine fuel mass flow rate with torque at 3500 rpm

Fig. 7 Parametric fitting of engine SFC.

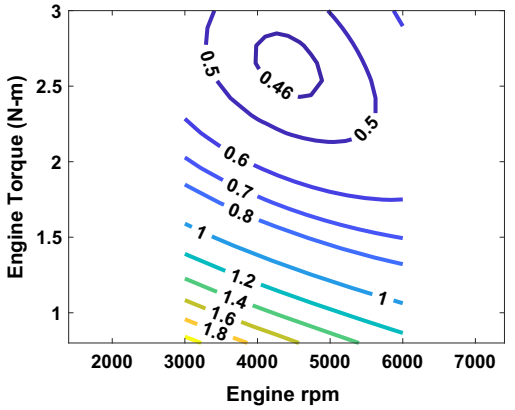

a) Engine SFC curve fit data contour

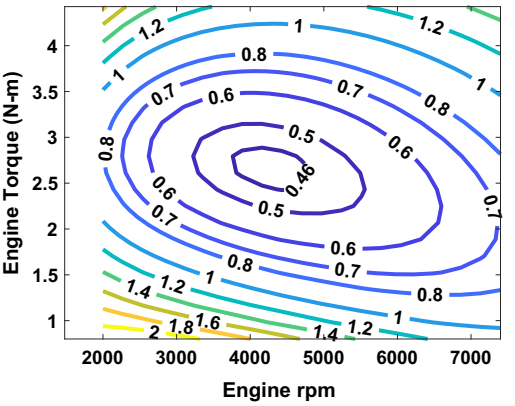

b) Engine SFC curve fit extrapolated data contour

Fig. 8 Measured engine SFC contour, in kilograms/kilowatt hour.

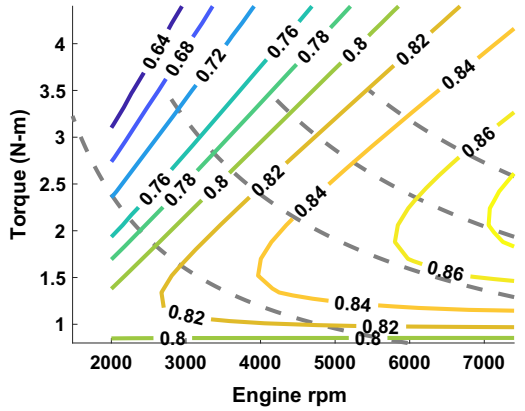

Fig. 10 Generator efficiency curve fit extrapolated data contour.

here on the engine SFC map. The derivation of the model begins from the power balance. The power input by the fuel is fuel mass flow rate $\dot{m}_f$, multiplied by the net calorific value (NCV). The indicated thermal efficiency η_T converts power input by the fuel to useful power called indicated power via combustion, $P_I = \eta_T \dot{m}_f NCV$. The indicated power consists of power output of the engine called brake power P_B, friction loss P_F, and pumping loss P_P. The pumping loss P_P is specific to a four-stroke engine. Thus, the power balance is

$$P_I = P_B + P_F + P_P \tag{1}$$

where

$$\eta_T \dot{m}_f NCV = P_I \tag{2}$$

The brake power is output torque times shaft speed $P_B = Q_E \Omega_E$. Another efficiency, the brake thermal efficiency η_B, converts the power input by the fuel directly to this power,

$$\eta_B \dot{m}_f NCV = P_B \tag{3}$$

Dividing Eq. (3) by Eq. (2) gives

$$\eta_B = \eta_T \left(\frac{P_B}{P_B + P_F + P_P} \right) = \eta_T \eta_M \tag{4}$$

The mechanical efficiency η_M converts indicated power to brake power. From Eq. (2), the fuel mass flow rate can be written as

$$\dot{m}_f = \frac{P_B}{\eta_T NCV} \left(1 + \frac{P_F + P_P}{P_B} \right) \tag{5}$$

The brake power P_B is related to the mean effective pressure inside the cylinder $bmep$. If the cylinder volume is V_S, the work done in one cycle is $bmep V_S$. If the engine speed is Ω_E in radians/second, $\Omega_E/(2\pi)$ is the number of revolutions per second; then, $\Omega_E/(2\pi n_c)$ is the number of cycles per second ($n_c = 2$ for a four-stroke engine). The work done per cycle times cycles per second is power, $P_B = bmep V_S \Omega_E/(2\pi n_c)$. Because $P_B = Q_E \Omega_E$, it follows that $bmep = 2\pi n_c Q_E / V_S$. The ratio of powers can be redefined as the ratio of equivalent mean effective pressures. Thus,

$$\dot{m}_f = \frac{Q_E \Omega_E}{\eta_T NCV} \left(1 + \frac{fmep + pmep}{bmep} \right) \tag{6}$$

and

$$bmep = \frac{2\pi n_c Q_E}{V_S} \tag{7}$$

In nondimensional form,

$$\overline{\dot{m}}_f = \frac{\dot{m}_f NCV}{Q_{E_{\max}} \Omega_{E_{\max}}} = \frac{\overline{Q}_E \overline{\Omega}_E}{\eta_T} \left(1 + \frac{fmep + pmep}{bmep} \right) \tag{8}$$

and

$$\overline{bmep} = \frac{bmep V_S}{Q_{E_{\max}}} = 2\pi n_c \overline{Q}_E \tag{9}$$

where the nondimensional engine torque is $\overline{Q}_E = (Q_E/Q_{E_{\max}})$ and nondimensional engine rpm is $\overline{\Omega}_E = (\Omega_E/\Omega_{E_{\max}})$. The variables $\dot{m}_f$, Q_E, and Ω_E are measured. NCV is known from the fuel used, and the swept cylinder volume V_S is known from the engine geometry. Thus, η_B is known at each test point. The goal is to find a functional representation of η_B in terms of Q_E and Ω_E.

We have from Eqs. (3) and (6)

$$\frac{1}{\eta_B} = \frac{1}{\eta_T} \left(1 + \frac{fmep + pmep}{bmep} \right) \tag{10}$$

The brake mean effective pressure is known in terms of Q_E but η_T, and the losses $fmep + pmep$ are not. These are very difficult to predict and where empirical data enter the model. Data from other four-stroke engine tests suggest that $(fmep + pmep)/bmep$ varies by third order in engine speed and inversely with engine torque [16,17]. Because $bmep$ is already a function of torque, we propose $fmep + pmep$ to have the following form:

$$fmep + pmep = A_0 + A_1 \overline{\Omega}_E + A_2 \overline{\Omega}_E^2 + A_3 \overline{\Omega}_E^3 \tag{11}$$

The problem now lies with η_T. The indicated thermal efficiency is normally a very complicated higher-order function of Q_E and Ω_E and can vary from engine to engine. Goering (in 1988) [18] proposed

$$\eta_T = \frac{\eta_{T0}}{1 + Q_E^n f(\Omega_E^4)} \tag{12}$$

Goering found for a two-stroke engine at low torque $\eta_T \approx \eta_{T0}$, where η_{T0} is a constant and f is a fourth-order polynomial in Ω_E. This was used to calibrate $fmep$ (two-stroke engines do not have separable pumping losses). However, this form was not found effective for the four-stroke model. Instead, we propose

$$\eta_T = \frac{1}{f(\overline{Q}_E^3) g(\overline{\Omega}_E^3)} \tag{13}$$

We found a torque and speed range where a simpler approximation held,

$$\eta_T \approx \frac{1}{b_0 + b_1 \overline{\Omega}_E + b_2 \overline{Q}_E} \tag{14}$$

This range was 2200–4500 rpm and 0.9–1.2 N · m. This range was used to calibrate $fmep + pmep$. For the purposes of that calibration,

$$\frac{1}{\eta_B} = \left(1 + \frac{A_0 + A_1 \overline{\Omega}_E + A_2 \overline{\Omega}_E^2 + A_3 \overline{\Omega}_E^3}{\overline{Q}_E} \right) (b_0 + b_1 \overline{\Omega}_E + b_2 \overline{Q}_E) \tag{15}$$

Once $A_0 - A_3$ are obtained, we revert back to the full expression of Eq. (13) to calibrate η_B over the entire engine range:

$$\frac{1}{\eta_B} = \left(1 + \frac{A_0 + A_1 \overline{\Omega}_E + A_2 \overline{\Omega}_E^2 + A_3 \overline{\Omega}_E^3}{\overline{Q}_E} \right) fg \tag{16}$$

Table 2 All model constants

Model constant	Calibrated value	Model constant	Calibrated value	Model constant	Calibrated value	Model constant	Calibrated value
A_0	0.0268	B_1	79.383	B_6	778.58	B_{11}	277.80
A_1	0.4552	B_2	−173.91	B_7	−389.13	B_{12}	57.691
A_2	−1.0207	B_3	127.72	B_8	−154.29	B_{13}	−226.90
A_3	0.8034	B_4	92.491	B_9	751.11	B_{14}	107.96
B_0	9.5011	B_5	−603.95	B_{10}	−718.54	B_{15}	−1.2802

$$fg = B_0 + B_1\overline{Q}_E + B_2\overline{Q}_E^2 + B_3\overline{Q}_E^3 + B_4\overline{\Omega}_E + B_5\overline{Q}_E\overline{\Omega}_E + B_6\overline{Q}_E^2\overline{\Omega}_E + B_7\overline{Q}_E^3\overline{\Omega}_E + B_8\overline{\Omega}_E^2 + B_9\overline{Q}_E\overline{\Omega}_E^2 + B_{10}\overline{Q}_E^2\overline{\Omega}_E^2 + B_{11}\overline{Q}_E^3\overline{\Omega}_E^2 + B_{12}\overline{\Omega}_E^3 + B_{13}\overline{Q}_E\overline{\Omega}_E^3 + B_{14}\overline{Q}_E^2\overline{\Omega}_E^3 + B_{15}\overline{Q}_E^3\overline{\Omega}_E^3 \quad (17)$$

The model constants are listed in Table 2. Because they are nondimensional and based on observed behavior of friction and pumping losses, we assume they are nominally representative of small scale four-stroke engines. The predicted fuel mass flow rate, specific fuel consumption, and brake thermal efficiency are plotted over the experimental data in Fig. 11. The trends are satisfactorily captured. The model can now be used in aircraft sizing.

The indicated thermal efficiency and mechanical efficiency obtained from the model are shown in Fig. 12. The losses are roughly 10–30% of the brake power at the nominal operating range of the engine. These losses are solely a function of engine speed. Friction increases at higher speeds. It is reasonable to expect friction force to be proportional to velocity, similar to a viscous damper, so power is proportional to Ω_E^2. Previous work also found that the friction losses can be approximated assuming a second-order function in engine speed [10,18]. It is assumed pumping force is proportional to velocity squared, similar to drag, so the pumping power is proportional to Ω_E^3.

The indicated thermal efficiency has similar islands as the brake efficiency except at high engine rpm. The mechanical efficiency in Fig. 12b shows that losses are highest at high engine speed, especially at low torque. Conversely, highest mechanical efficiency is seen at low engine speed and high torque. Although the mechanical efficiency obtained from the data is reasonable, the indicated thermal efficiency is fairly low. The maximum thermodynamic efficiency of an Otto cycle with a compression ratio of 5 is roughly 45%. Accounting for real world inefficiencies, the maximum attainable indicated thermal efficiency drops to about 30% [19], again for a compression ratio of 5, similar to the engine used in these experiments. The additional losses to indicated thermal efficiency from these experiments are explained by suboptimal operating temperature of the engine as well as tuning of the carburetor. The carburetor needed to be tuned such that the engine could operate at the widest range of speed and torque possible. The high- and low-speed needles were fixed for the experiments, thereby sacrificing performance at a specific operating condition. Therefore, the indicated thermal efficiency obtained from the model is reasonable.

VI. Aircraft Sizing

The engine model is now integrated with VTOL aircraft sizing to understand its impact. Aircraft sizing calculates a consistent combi-

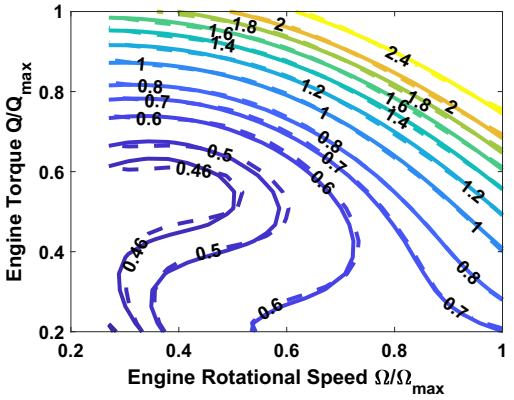

a) Contour of fuel mass flow rate

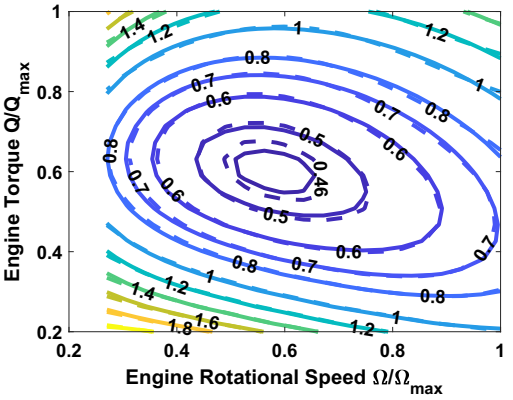

b) Contour of specific fuel consumption (SFC)

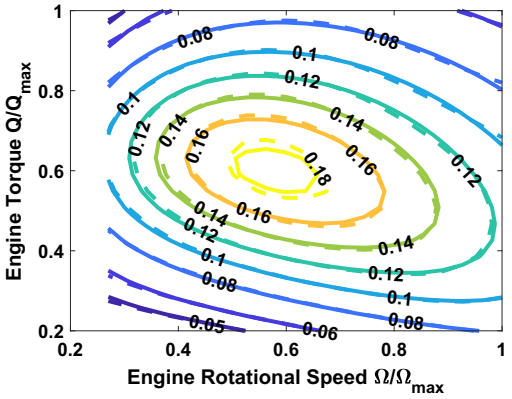

c) Contour of brake thermal efficiency η_B

Fig. 11 Agreement between predictions (dashed) and experiment (solid).

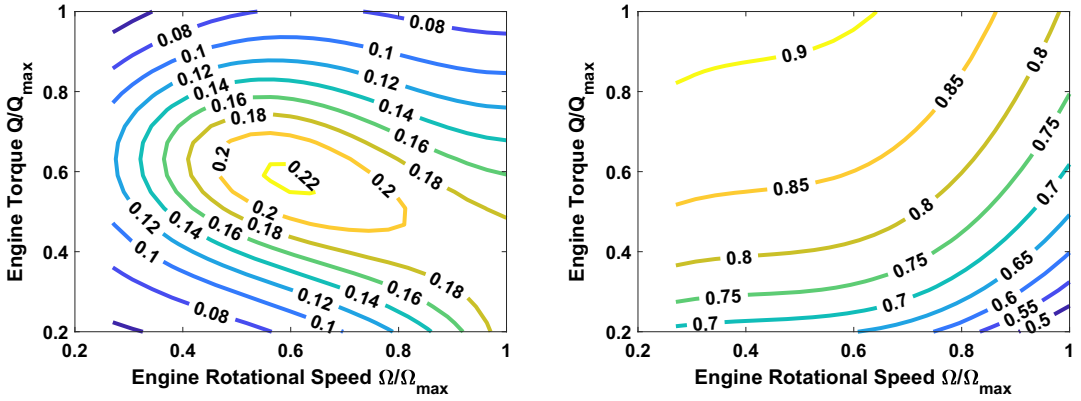

a) Contour of indicated thermal efficiency η_T b) Contour of mechanical efficiency η_M

Fig. 12 Predictions of indicated thermal efficiency and mechanical efficiency.

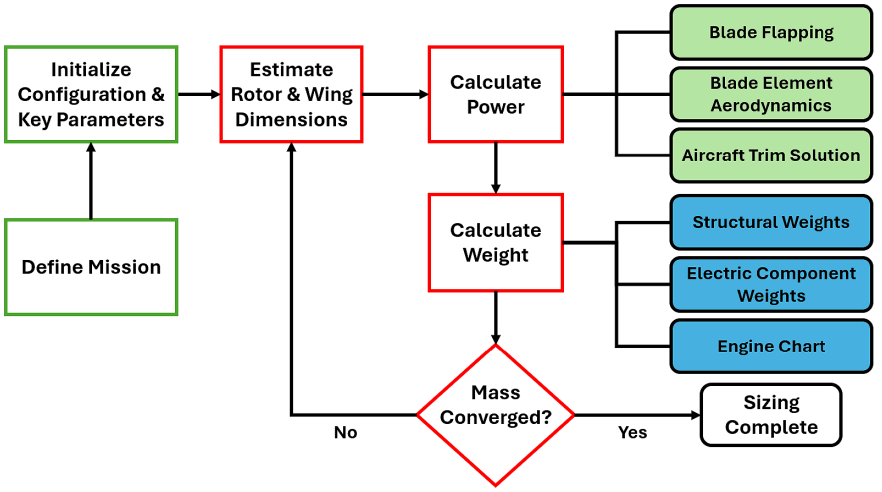

Fig. 13 Sizing methodology.

nation of gross vehicle dimensions, select operating parameters, component empty weights, and mission fuel that allow a vehicle to perform a given mission profile. The mission profile may consist of different combinations of range and payload. A typical sizing workflow is shown in Fig. 13, similar to that in Ref. [9]. The key elements are calculation of rotor and powertrain performance, component empty weights, and fuel burn throughout the mission. This order of calculations results in minimum iterations to converge to a consistent solution. Calculating power accurately requires blade flapping, blade element airloads with airfoil decks, uniform inflow, and a trim solution. Calculation of weights are difficult and rely on historical regression models or data from successful full-scale flight-test articles.

A. Calculation of Power

There are no flight-test data on the QBIT configuration, so the performance calculations are validated with data from XV-15 flight testing [20]. The predicted aircraft L/D is shown against airspeed in Fig. 14. The XV-15 was in forward flight mode for these tests, that is, pylons tilted fully forward. To find power, drag must be approximated. The equivalent flat plate area of the XV-15 was approximated by $D/q = k\,(W/1000)^{2/3}$ with $k = 1.16$ and does not include the

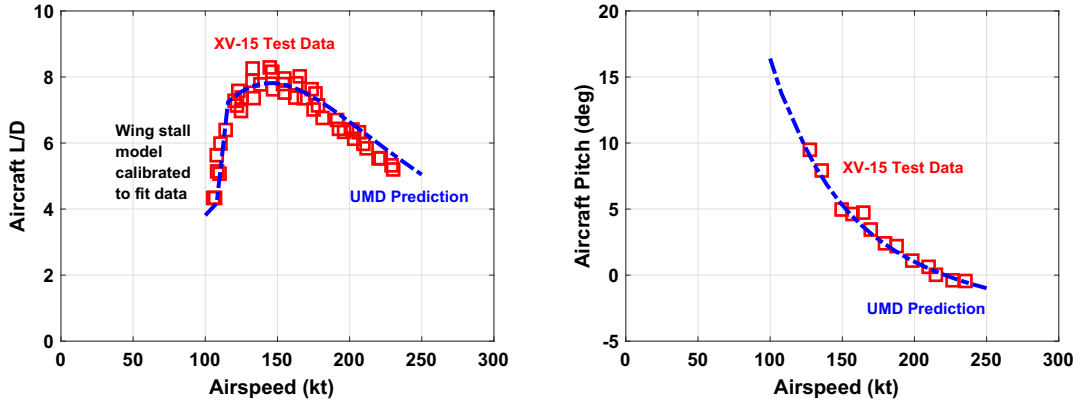

a) Total aircraft L/D in cruise b) Vehicle trim pitch attitude (positive nose-up)

Fig. 14 Prediction of XV-15 cruise performance (UMD, University of Maryland).

profile drag from the wings. The wing profile drag is calculated with angle of attack.

Figure 14a shows aircraft lift-to-drag ratio, $L/D = Wa_G v/P$, where W is the gross weight, a_G is the acceleration due to gravity, v is the cruise velocity, and P is aircraft cruise power. The cruise power required is inclusive of transmission efficiency and accessory losses; thus, overall aircraft L/D is represented and not equivalent rotor L/D. Figure 14b shows the nose-up pitch attitude. Wing airfoil properties are not available in the public domain, so a simple stall model is used and calibrated to best fit the sudden drop in L/D below 120 kt. It is an artificial addition to the wing drag coefficient by $2\alpha^2$ at angles of attack above 16 deg.

B. Calculation of Weights

The U.S. Army Aeroflightdynamics Directorate (AFDD) weight models are used for the XV-15, and technology factors are used to match detailed aircraft data obtained from NASA Ames Research Center. For the QBIT, structural weight models were used from AFDD (e.g., fuselage, wing, rotor, etc.), while the propulsion system weights were taken from Ref. [21]. The weight models for these components were developed in house from commercially available data on small engines, electric motors, and inverters. These regression models are shown in Fig. 15 with the formulas obtainable from Ref. [21]. Weight is in kilograms, power is in kilowatts, and torque is in N · m.

In the absence of full-scale battery-electric aircraft data, the model is verified with a conceptual design published by NASA [22]. The conceptual aircraft is a battery powered quadcopter with disk loading of 2.5 lb/ft^2, payload of 250 lb, cruise speed of 70 kt, 5 min hover, and cruise reserve of 20 min. Similar to the XV-15, the equivalent flat plate area was approximated by $D/q = k\,(W/1000)^{2/3}$ but with $k = 2.95$. This is to account for the additional features and structural interfaces between the fuselage, wings, and boom structures resulting in a design that is not as aerodynamic as the XV-15. Verification of these models is shown in Fig. 16. With

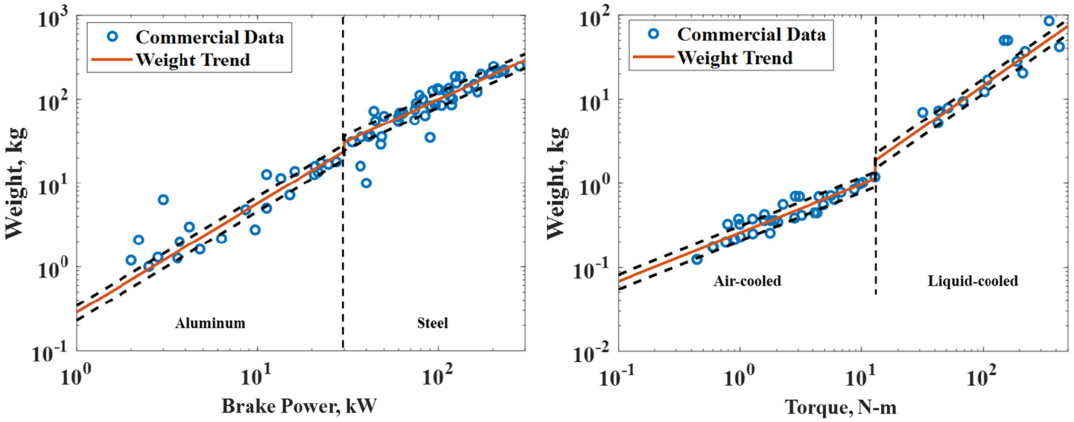

a) Engine weight model

b) Electric motor weight model

c) Inverter weight model

Fig. 15 Propulsion system weight models; 20% error bounds.

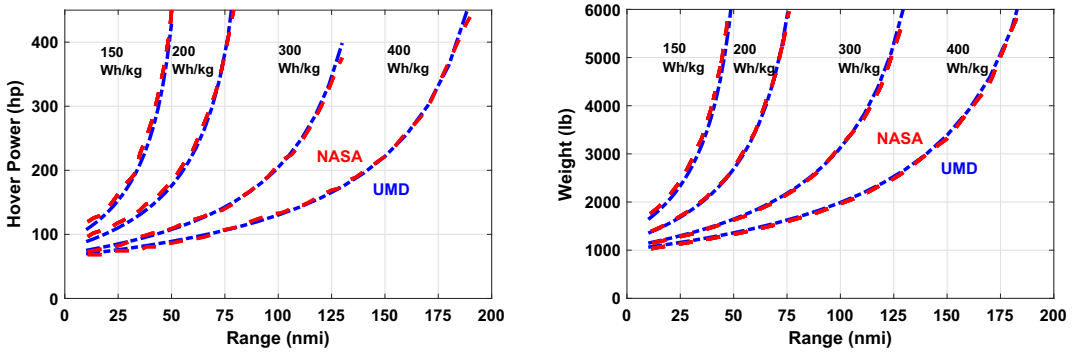

a) Hover power prediction of NASA electric quadrotor

b) Gross weight prediction of NASA electric quadrotor

Fig. 16 Predicted hover power and gross weight of NASA conceptual battery-electric quadrotor.

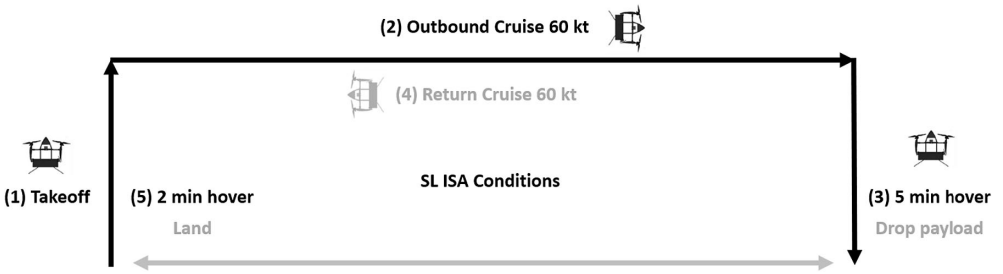

Fig. 17 Sizing mission; payload 5 lb.

Table 3 Fixed aircraft parameters

Rotors	4
Blades	2
Disk loading	2.76 lb/ft^2
Solidity (per rotor)	0.1
V_{tip}(Hover)	328 ft/s
Wings	2
Wing loading	7.43 lb/ft^2
Wing aspect ratio	10

these, the performance and weight models needed for our QBIT are considered verified.

VII. Sizing Results: Hybrid-Electric QBIT

With all models verified, a sizing study is conducted for the QBIT. The mission is kept deliberately simple as shown in Fig. 17. The payload is 5 lb, and the cruise speed is 60 kt. The fixed aircraft parameters are shown in Table 3. The powertrain sizing parameters are not fixed, with power and torque driving the weights of the engine and electric motors, respectively. Additionally, a constant transmission efficiency of 85% is assumed based on the generator efficiency shown earlier. The rotor tip speed in hover is the nominal rotor tip speed (NR). The tip speed reduction in cruise is swept manually from 100% NR to 35% NR.

Figure 18 shows the difference between L/D of the XV-15 and the QBIT. The expected L/D of the QBIT is much lower than the XV-15, primarily due to low Reynolds number effects at the design cruise speed. As a reminder, reducing the tip speed in forward flight can lead to dramatic increases in L/D. The optimal tip speed reduction must be determined. The 50 lb QBIT is modeled and trimmed for varying tip speed reduction using a Blade Element Momentum Theory (BEMT) aerodynamic analysis. The predicted L/D of this aircraft at a fixed cruise speed of 60 kt is shown in Fig. 19. The best L/D is achieved at 40% NR. The question is whether 40% NR is still the best tip speed reduction when the engine SFC model is added.

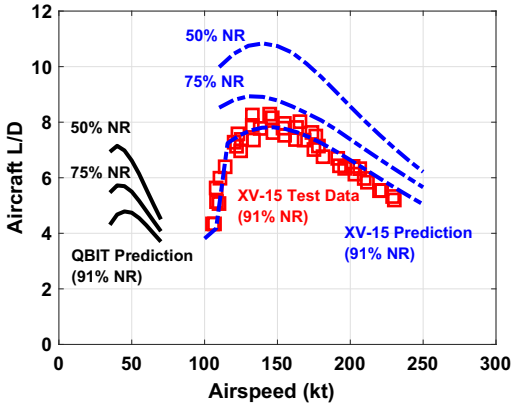

Fig. 18 L/D versus speed of XV-15 and QBIT.

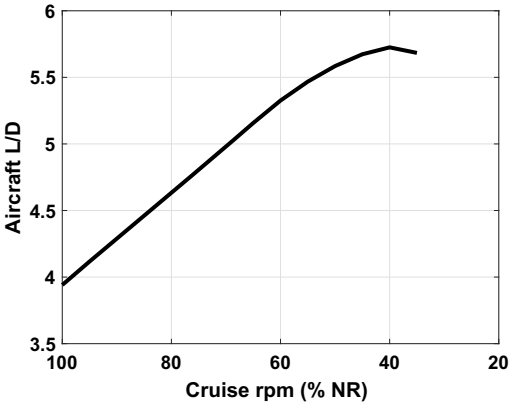

Fig. 19 QBIT L/D versus tip speed reduction in cruise.

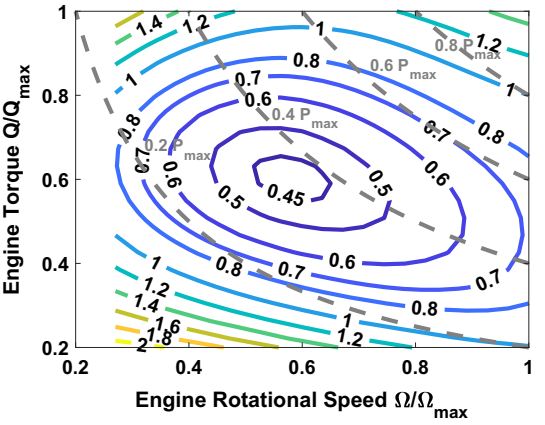

Fig. 20 Engine SFC contours with constant power lines marked.

Although many of the aircraft parameters are fixed, the engine sizing parameters are not. The engine model is shown in Fig. 20. The maximum engine rpm $\Omega_{E_{max}}$ is set to 7400. The engine speed sets the bus voltage and is assumed to follow the rotor speed; that is, if the rotor rpm is dropped to 50% NR, the engine rpm is also dropped to 50% NR. This method of control mimics how a mechanically connected engine would operate and serves as the baseline mode rpm reduction. Additional modes of rpm reduction are discussed in Sec. VIII. The maximum engine torque is calculated in each sizing iteration. The torque required from the engine is found for each mission segment. The maximum torque throughout the mission is set to equal 90%$Q_{E_{max}}$. Because the maximum engine rpm is fixed, allowing the maximum torque to change is what allows the engine contour to scale with power. The weights of the powertrain components and fuel consumed are the core variables in this sizing study.

The QBIT is first sized using the detailed engine model with a cruise tip speed of 100% NR, shown in Fig. 21a. Then, the vehicle is sized assuming a cruise tip speed of 40% NR with the expectation of maximizing L/D, shown in Fig. 21b. The detailed model shows rpm reduction to 40% NR in cruise increases gross weight despite higher

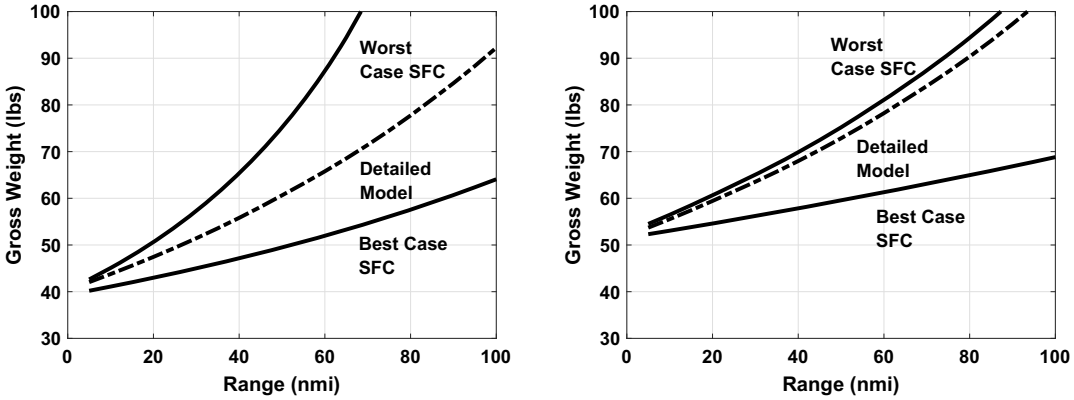

a) Cruise rpm =100% NR b) Cruise rpm = 40% NR

Fig. 21 Comparing three methods of assuming SFC in a sizing exercise.

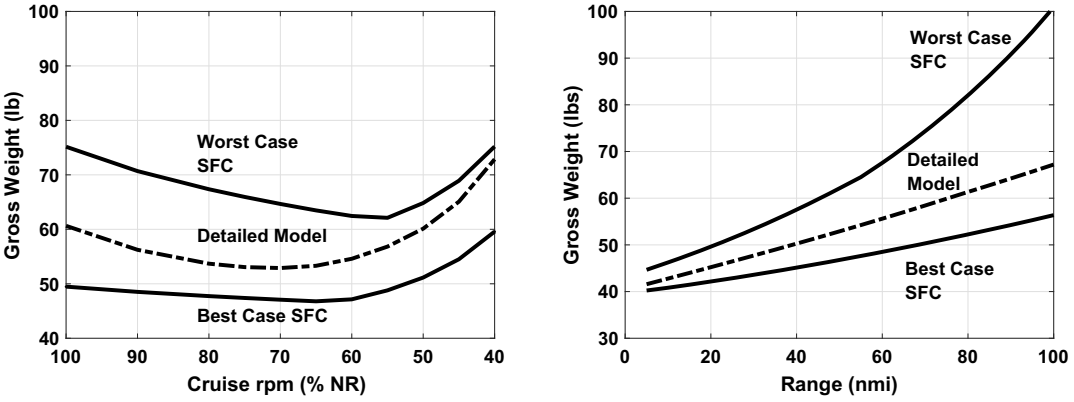

a) Weight versus tip speed reduction b) Weight versus range

Fig. 22 Sizing with best tip speed reduction.

L/D. The increase in SFC more than offsets the gains from aircraft L/D through increase in fuel consumption. Additionally, the cruise torque becomes higher than hover, which increases the size of the electric motors and engine. The weights of the propulsion components and fuel consumed are quite sensitive to how the engine supplies the necessary power. Thus, aerodynamic performance must be balanced with engine performance and torque requirements. A sensitivity analysis is performed by also sizing the aircraft assuming best-case and worst-case scenarios for engine SFC, according to the SFC map. The minimum gross weight is predicted with varying range for each case, shown in Fig. 21 for 100% NR and Fig. 21b for 40% NR. The detailed model is clearly important for proper assessment of gross weight. Notably, if the cruise rpm is dropped to 40% NR, a 50 lb QBIT is not possible even assuming best-case scenario for SFC.

Figure 22 illustrates sizing with proper tip speed reduction considering both aerodynamics and the engine. In Fig. 22a, the range is fixed to 50 nmi (nautical miles). The gross weight is predicted for the three SFC cases as before. Below 70% NR, no performance benefits for rpm reduction were observed when including the more detailed SFC model, indicating the vehicle weight is very sensitive to SFC. In Fig. 22b, the gross weight is predicted again for the same three cases, but now the tip speed is reduced by different amounts in each case. The ranged predicted for a 50 lb vehicle is about 37 nmi.

VIII. Modes of RPM Reduction

So far, it has been assumed that the engine rpm was reduced proportionally to rotor rpm. Are there more efficient modes of rpm reduction? Recall Fig. 2 in which only one motor is shown for clarity. The rotor rpm and torque required will dictate the voltage and current drawn by the motor, respectively, which in turn will dictate the engine rpm and torque.

Consider three cases:

1) For rpm scaling, the engine rpm is proportional to the rotor rpm. This is the baseline case analyzed in the previous section.

2) For constant rpm, the engine rpm is fixed to the hover value.

3) For minimum SFC, the engine rpm is independent of rotor rpm. The engine rpm is selected to minimize SFC.

Direct-current-to-alternating-current inverters, also known as motor controllers, are capable of modifying the duty cycle of the control signal passed to the electric motors to reduce the mean voltage the motor receives, reducing rpm. Typically, they are designed to operate only as buck converters, not boost. The motor voltage could be made to exceed the bus voltage using a technique called field weakening. However, because of its reduced torque and complex control requirements, the capability of field weakening is neglected, and a limitation is set such that the bus voltage may not drop below the voltage the motors require. Field weakening is meant to achieve higher speeds, not lower, as in the design case.

The voltage of the signal from the controller controls the motor rpm, allowing the controller to adjust the rotor rpm independently of the engine as long as the voltage supply is greater than or equal to the voltage required of the motor. Of course, power is conserved through the controller, minus inherent losses, so if the voltage is reduced through duty cycle, the current is increased. This is accomplished through a strategically sized combination of an inductor and a capacitor. When the signal is on, current flows to the load through the inductor generating a magnetic field and charging the capacitor. When the signal is off, the polarity of the inductor reverses, and the magnetic field collapses, releasing the energy stored in it as current, while the stored charge in the capacitor ensures a constant voltage. In essence, the load is driven by the stored energy in the inductor and capacitor and not by the power source.

Consider an example illustrated in Fig. 23. For the sake of illustration, consider the transmission efficiency to be 1. The engine

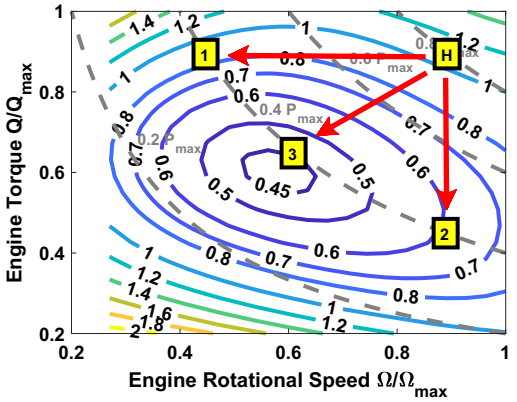

Fig. 23 Engine rpm reduction from hover to cruise for three control cases.

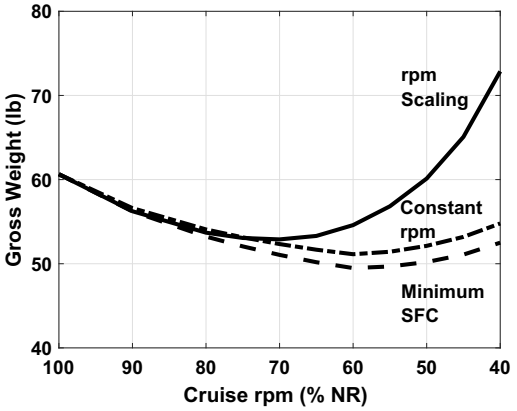

Fig. 24 Impact of tip speed reduction on takeoff weight.

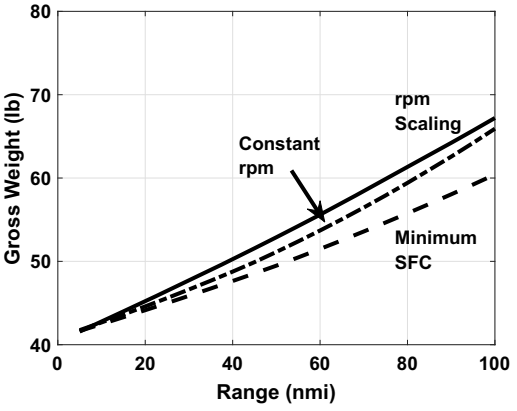

Fig. 25 Sized vehicle takeoff weight for different powertrain operating modes.

is sized such that hover power is supplied at $0.9\,\Omega_{E_{\max}}$ and $0.9\,Q_{E_{\max}}$, resulting in an engine operating point at $0.81P_{E_{\max}}$. Assume that the optimal cruise power for the rotors is half the hover power. To obtain this cruise power, say the rotor rpm is reduced by 50%. As rpm is directly related to voltage, the voltage is reduced by 50%. Because the engine power is directly proportional to the rotor power, the engine operating point in cruise must be somewhere along the constant power line at $0.4\,P_{E_{\max}}$. In the case of rpm scaling, the engine rpm drops at the same rate as rotor rpm, resulting in half of the original engine rpm. In this case, the bus voltage is exactly what the rotor needs. Additionally, the torque required in cruise is equal to the torque in hover. This constant torque operation falls out from this particular combination of power and rpm ratio and does not represent any constraint on the engine operating condition. In the case of a constant rpm, the bus voltage is much higher than the voltage the motor requires in cruise; thus, the controller manages the rotor rpm and torque by reducing signal voltage and boosting the current. In the case of minimum engine SFC, the engine rpm is swept at the power required, and the point of minimum SFC is determined. The resulting bus voltage is higher than the rotor requires, so the controller, once again, reduces voltage and boosts current. In this case, the limit on rpm reduction of the engine equals the drop in rotor rpm. This is the limitation on bus voltage.

To understand how each case impacts sizing, we return to the design problem. Figure 24 shows the impact of tip speed on gross weight for a range of 50 nmi. All the cases use the detailed SFC model. RPM scaling is identical to the detailed SFC line in Fig. 22a earlier. Although reducing the rotor tip speed showed no benefit below 70% NR before, a benefit is seen for the other modes of engine rpm reduction down to 60% NR. Minimizing SFC is clearly the most effective way to minimize fuel burn and weight. This strategy achieves minimum fuel consumption and allows the motor controller to regulate voltage and current to the rotors appropriately. Operating at a constant rpm, which provides the simplest method of control, also displays a clear benefit with tip speed reduction. The voltage and current management come entirely from the motor controller. The best tip speed reduction for rpm scaling is 70% NR, and the other cases are 60% NR.

With the best tip speeds selected, the aircraft weight for each case is shown in Fig. 25. The vehicle range varies from 37 to 53 nmi depending on how the engine is controlled. Managing the engine speed to operate at minimum SFC and using the motor controller to manage rotor speed achieves the highest range of 53 nmi for a 50 lb vehicle. Fixing the engine rpm greatly simplifies the control scheme but reduces range to around 45 nmi. Dropping the engine rpm at the same rate as the rotor rpm may simplify the control scheme but is the worst of all and results in the lowest range of around 37 nmi. Minimizing the engine fuel consumption results in the longest range aircraft; thus, the engine rpm should be independently controlled to minimize its fuel consumption at the required power output. Then, the motor controllers are responsible for manipulating that power and supplying the correct voltage and current to the rotors. The empty weight fraction calculated from the AFDD and in-house weight models is about 0.82 for all cases and $L/D \approx 4.2$–4.6. The three operating modes are summarized in Table 4.

IX. Conclusions

Experiments were conducted on a hybrid-electric powertrain using a 3.43 kW IC (internal combustion) engine, and component-level performance data were gathered for the engine/generator combination. A powertrain efficiency model was synthesized from the data. The model captures sensitivities to the engine operating conditions. This model was rubberized for quantifying variations in engine efficiency with operating torque and rpm

Table 4 Key results of operating modes

Operating mode	Constraints	Free parameter (s)	Complexity	Range difference, %
RPM scaling	Engine rpm is fixed to follow rotor rpm	Rotor rpm	Baseline, similar to mechanical operation	0
Constant rpm	Engine rpm is fixed to hover value	Rotor rpm	Less complex	+16
Minimum SFC	Minimum engine rpm limit is equal to reduction in rotor rpm	Rotor rpm engine rpm	More complex	+43

in a scale-invariant manner and integrated into an in-house aircraft sizing analysis. A 50 lb QBIT was sized, and a sensitivity analysis conducted to quantify the impact of engine SFC assumptions. Several methods of engine control to meet the rotor operating torque and speed combinations were detailed and compared to one another in complexity and value. Based on this work, the following key conclusions are drawn:

1) A detailed SFC map as a function of torque and speed is needed for proper sizing of VTOL aircraft where rotor rpm is a key performance parameter.

2) The engine efficiency map is complicated due to high orders of nonlinearities in indicated thermal efficiency that is well represented by a third-order polynomial fit in torque and engine speed and friction and pumping losses that are well represented by second- and third-order fits in engine speed.

3) Without an engine SFC map that captures the variation in speed and torque separately, optimal tip speed reduction in cruise (a key attribute and benefit of distributed propulsion) is predicted incorrectly during sizing. A 60% tip speed reduction is predicted in cruise without a detailed engine SFC model, whereas, depending on the method of rpm control, the percent reduction for minimum weight is between 30 and 40%. Thus, an error of 50% in tip speed reduction may occur.

4) The reduction in tip speed for cruise must be judiciously selected to balance rotor performance with engine performance. Maximizing aircraft L/D based on rotor aerodynamics alone will not lead to minimum gross weight.

5) Without a detailed SFC model, maximum range for a given gross weight is predicted incorrectly by sizing. For example, for a 50 lb gross weight QBIT, ranges from 20 to 65 nmi may be predicted using best-case and worst-case assumptions for engine SFC, whereas the correct range is 37 nmi. Thus, errors of 50–100% in range prediction may occur.

6) Reduction in rotor tip speed should not be carried out by motors alone. The engine should also be controlled independently to minimize the fuel consumed at the desired power output. Complexity is added to the control scheme, but significant operational gains can be attained.

7) The maximum range 50 lb QBIT is designed by operating the engine at minimum SFC for a desired power output. For this vehicle, the gross weight is very sensitive to increases in SFC, despite increases in L/D. The range of the 50 lb vehicle is extended by 43% relative to the baseline control configuration of matching the engine and rotor speed changes. Other options are possible that trade complexity for capability, but minimum weight is achieved by operating at minimum SFC at a desired power within bus voltage limitations.

Acknowledgments

This work was carried out at the Alfred Gessow Rotorcraft Center University of Maryland at College Park under the U.S. Army/Navy/NASA Vertical Lift Research Center of Excellence grant number W911W62120003 with technical monitoring from Michael Vegh, David Friedmann, and Mahendra Bhagwat (U.S. Army Combat Capabilities Development Command (DEVCOM), Aviation & Missile Center (AvMC)). The authors are also grateful to Brent Mills (U.S. Army DEVCOM, DEVCOM Analysis Center (DAC)) for his advice and guidance.

References

[1] Dean, F., *Curtiss X-Planes: Curtiss-Wright's VTOL Effort 1958-1965*, Schiffer Military History Book Series, Schiffer Publ., Atglen, PA, 2001.

[2] Schuler, J. M., Smith, R. E., and Lebacqz, J. V., "An Experimental Investigation of STOL Longitudinal Flying Qualities in the Landing Approach Using the Variable Stability X-22A Aircraft," *Proceedings of 28th Annual National Forum of the American Helicopter Society*, Vertical Flight Soc., May 1972.

[3] Husain, I., *Electric and Hybrid Vehicles: Design Fundamentals*, 3rd ed., CRC Press, Taylor & Francis Group, Boca Raton, FL, 2021. https://doi.org/10.1201/9780429490927

[4] Mi, C., and Masrur, M. A., *Hybrid Electric Vehicles: Principles and Applications with Practical Perspectives*, 2nd ed., Wiley, Hoboken, NJ, 2018. https://doi.org/10.1002/9781118970553

[5] Friedrich, C., and Robertson, P., "Hybrid-Electric Propulsion for Aircraft," *Journal of Aircraft*, Vol. 52, No. 1, 2015, pp. 176–189. https://doi.org/10.2514/1.C032660

[6] Dehesa, D., Menon, S., Brown, S., and Hagen, C., "Dynamic Analysis of a Series Hybrid-Electric Powertrain for an Unmanned Aerial Vehicle," *Journal of Propulsion and Power*, Vol. 38, No. 1, 2022, pp. 84–96. https://doi.org/10.2514/1.B38261

[7] Lee, D., Lim, D., and Yee, K., "Generic Design Methodology for Vertical Takeoff and Landing Aircraft with Hybrid-Electric Propulsion," *Journal of Aircraft*, Vol. 59, No. 2, 2021, pp. 278–292. https://doi.org/10.2514/1.C036214

[8] Warwick, G., "SureFly Electric Helicopter Achieves First Flight," Aviation Week, May 2018.

[9] Sridharan, A., Govindarajan, B., and Chopra, I., "A Scalability Study of the Multirotor Biplane Tailsitter Using Conceptual Sizing," *Journal of the American Helicopter Society*, Vol. 65, No. 1, 2020, pp. 1–18. https://doi.org/10.4050/JAHS.65.012009

[10] Mills, B., and Datta, A., "Fundamental Studies of Variable-Voltage Hybrid-Electric Powertrains," *Journal of the American Helicopter Society*, Vol. 66, No. 2, 2021, pp. 1–14. https://doi.org/10.4050/JAHS.66.022009

[11] Ricci, M., Varahamurthy, V., and Hicks, R., "Power System Characterization and Flight Testing of a >55 lb Hybrid-Electric Multirotor," *Vertical Flight Society Annual Forum 78*, Vertical Flight Soc., May 2022. https://doi.org/10.4050/F-0078-2022-17529

[12] Arace, M., and Datta, A., "Fundamental Understanding of Hybrid-Electric Power," *Vertical Flight Society Annual Forum 79*, Vertical Flight Soc., May 2023. https://doi.org/10.4050/F-0079-2023-18061

[13] Arace, M., and Datta, A., "Impact of Detailed SFC on Hybrid-Electric VTOL Sizing," *Vertical Flight Society Annual Forum 80*, Vertical Flight Soc., May 2024. https://doi.org/10.4050/F-0080-2024-1341

[14] Mistry, M., and Gandhi, F., "Helicopter Performance Improvement with Variable Rotor Radius and RPM," *Journal of the American Helicopter Society*, Vol. 59, No. 4, 2014, pp. 1–19. https://doi.org/10.4050/JAHS.59.042010

[15] Sadeghi, S., and Parsa, L., "Multiobjective Design Optimization of Five-Phase Halbach Array Permanent-Magnet Machine," *IEEE Transactions on Magnetics*, Vol. 47, No. 6, 2011, pp. 1658–1666. https://doi.org/10.1109/TMAG.2011.2106217

[16] Kumar, P. S., Venkatesh, B., Rajeswari, B., Reddy, V. L., and Khan, S. P., "Emission Control by Using Water Emulsified Diesel in Single Cylinder Diesel Engine," *International Journal of Advances in Engineering & Technology*, Vol. 5, No. 2, 2013, pp. 263–273.

[17] Hatte, P., and Bhalerao, Y., "Influence of Ethanol-Gasoline Fuel Fractions on Variable Compression Ratio Engine," *International Journal of Recent Technology and Engineering*, Vol. 8, No. 3, 2019, pp. 2929–2936. https://doi.org/10.35940/ijrte.C4792.098319

[18] Goering, H. C., "Engine Model for Mapping BSFC Contours," *Mathematical and Computer Modelling*, Vol. 11, 1988, pp. 514–518. https://doi.org/10.1016/0895-7177(88)90546-8

[19] Marks, L. S., Goodenough, G. A., Baker, J. B., Allcut, E. A., Lichty, L. C., Cross, C. N., Upton, G. B., Schweitzer, P. H., Kates, E. J., Ellenwood, F. O., et al., "Discussion: "Efficiencies of Otto and Diesel Engines" (Ellenwood, F. O., Evans, F. C., and Chwang, C. T., 1928, Trans. ASME, 49-50(9), p. 091005),," *Transactions of the American Society of Mechanical Engineers*, Vols. 49–50, No. 9, 2023, Paper 091005. https://doi.org/10.1115/1.4058841

[20] Johnson, W., "NDARC—NASA Design and Analysis of Rotorcraft Validation and Demonstration," *AHS Aeromechanics Specialists' Conference*, Vertical Flight Soc., NASA ARC-E-DAA-TN1109, Jan. 2010.

[21] Mills, B., "Fabrication and Fundamental Studies of a 4-kW, Variable-Voltage, Distributed Hybrid-Electric Powertrain for eVTOL Aircraft," Ph.D. Thesis, Univ. of Maryland, College Paerk, MD, 2022.

[22] Johnson, W., Solis, E., and Silva, C., "Concept Vehicles for VTOL Air Taxi Operations," *TVF*, Vertical Flight Soc., ARC-E-DAA-TN50731, Jan. 2018.

I. Chopra
Associate Editor